Theory and experimental validation of cross-flow micro-channel heat exchanger module with reference to high Mach aircraft gas turbine engines

Robert Nacke, Brittany Northcutt, Issam Mudawar *

Boiling and Two-Phase Flow Laboratory (BTPFL), Purdue University International Electronic Cooling Alliance (PUIECA), Mechanical Engineering Building, 585 Purdue Mall, West Lafayette, IN 47907, USA
Rolls-Royce Purdue University Technology Center (UTC) in High Mach Propulsion, Maurice Zucrow Laboratories, 500 Allison Road, Purdue University, West Lafayette, IN 47907, USA

ARTICLE INFO

ABSTRACT

This study explores the design, analysis, and performance assessment of a new class of heat exchangers intended for high Mach aircraft gas turbine engines. Because the compressor air that is used to cool turbine blades and other components in a high Mach engine is itself too hot, aircraft fuel is needed to precool the compressor air, cooling is achieved with a new heat exchanger. The heat exchanger consists of a large number of miniature, closely-spaced modules. Within each module, the fuel flows through a series of parallel micro-channels, while the air flows externally over rows of short, straight fins perpendicular to the direction of fuel flow. A theoretical model was developed to predict the thermal performance of the module for various operating conditions. To confirm the accuracy of the model, a single module was constructed and tested using water to simulate the aircraft fuel. The theoretical model was used to predict the air temperature drop, water temperature rise, and heat transfer rate for each fluid stream. Comparisons between theory and experiment show good overall agreement in exit temperatures and heat transfer rates. This study shows the theoretical model is a reliable tool for predicting the performance of heat exchanger modules under actual fuel and air turbine engine conditions and for the design of aircraft heat exchangers of different sizes and design envelopes.

© 2010 Elsevier Ltd. All rights reserved.

1. Introduction

Supersonic gas turbine engines pose unique thermal management challenges not encountered in subsonic engines. In both cases, compressor bleed air is used to cool various downstream engine components such as turbine blades. For subsonic engines, the compressor bleed air is cool enough to be used directly to cool the turbine blades [1]. However, for supersonic engines, the compressor bleed air temperature is quite high and a heat exchanger is needed to precool the air before it is introduced to the turbine blades.

Cooling of the compressor bleed air can be achieved by rejecting heat to either the engine fan's bypass air or the fuel [2,3]. In some cases, depending on engine cycle requirements and thermal management architecture, using fuel as the heat sink may allow a more compact and lightweight heat exchanger than using air.

Previous efforts to optimize air–fuel heat exchanger design have been focused on investigating heat transfer schemes for the air and the fuel sides individually. Most heat exchanger designs involve flow of compressor bleed air across a series of circular tubes carrying the cooler fuel, similar to what is typically encountered in a conventional shell-and-tube heat exchanger. Huang et al. [3] used metal foam to enhance heat transfer on the airside. Their tests revealed that foam is too heavy for turbine engines and recommended that other designs with better heat capacity-to-weight ratios be developed. Kibbey [4] investigated the merits of enhancing heat transfer on the fuel side by fitting the circular fuel tube with an inner coaxial tube that featured holes to supply jets of fuel against the wall of the outer tube. While jet impingement did produce high convective heat transfer coefficients, interactions between the jets and the spent fuel flow in the annulus between the two tubes, as well as the need to utilize a large number of closely spaced jets, rendered this design impractical and inefficient. Herring and Heister [5] also investigated heat transfer enhancement on the fuel side by inserting wire coils inside the fuel tubes. The inserts provided appreciable fuel-side heat transfer enhancement with JP-10 jet fuel, but still further enhancement is desired.

Developing a fuel–air heat exchanger that is more compact, lightweight and effective than current cross-flow topologies is the primary motivation for this work. The new heat exchanger is comprised of many modules that can be arranged to suit a variety of engine envelopes. Fig. 1(a) illustrates the basic construction of a

* Corresponding author at: Boiling and Two-Phase Flow Laboratory (BTPFL), Purdue University International Electronic Cooling Alliance (PUIECA), Mechanical Engineering Building, 585 Purdue Mall, West Lafayette, IN 47907, USA. Tel.: +1 (765) 494 5705; fax: +1 (765) 494 0539.
E-mail address: mudawar@ecn.purdue.edu (I. Mudawar).

Nomenclature

A	airside parameter defined in Eq. (5a)
$A_{c,csf}$	fuel (or water) fin cross-sectional area
$A_{h,csf}$	air fin cross-sectional area
$A_{h,f}$	airside finned area
$A_{h,uf}$	airside unfinned area
b	fuel-side (or waterside) parameter defined in Eq. (5b)
c_p	specific heat at constant pressure
$D_{c,eq}$	fuel-side (or waterside) micro-channel hydraulic diameter
$D_{h,eq}$	airside hydraulic diameter on back of module
$H_{c,ch}$	fuel-side (or waterside) micro-channel height
$H_{c,w}$	module's outer wall thickness
$H_{h,f}$	airside fin height
$H_{h,fe}$	corrected airside fin height
$\bar{h}_c$	average fuel-side (or waterside) heat transfer coefficient
$\bar{h}_{h,b}$	average airside heat transfer coefficient on back of module
$\bar{h}_{h,f}$	average airside fin heat transfer coefficient
$\bar{h}_{h,uf}$	average airside heat transfer coefficient along surface between fins
k_c	thermal conductivity of fuel (or water)
k_h	thermal conductivity of air
k_s	thermal conductivity of heat exchanger module
L	length of module in direction of fuel (or water) flow
$L_{h,f}$	airside fin length
m_c	fuel-side (or waterside) fin parameter
m_h	airside fin parameter
$\dot{m}_c$	fuel (or water) mass flow rate
$\dot{m}_h$	air mass flow rate
$N_{c,ch}$	number of fuel-side (or waterside) micro-channels
$N_{h,f}$	number of airside fin rows
$N_{h,r}$	number of small fins in airside fin row
$\overline{Nu}_c$	average fuel-side (or waterside) Nusselt number
$\overline{Nu}_{h,b}$	average airside Nusselt number on back of module
$\overline{Nu}_{h,f}$	average airside Nusselt number on finned side of module along fins
$\overline{Nu}_{h,uf}$	average airside Nusselt number on finned side of module between fins
$P_{c,f}$	fuel (or water) fin perimeter
$P_{h,f}$	air fin perimeter
Pr	Prandtl number
q	heat exchanger module's heat transfer rate
q''	heat flux across module
$q_{a,b}$	back surface heat transfer rate
$q_{c,exp}$	measured water side heat transfer rate
$q_{c,th}$	theoretical water side heat transfer rate
$q_{c,sw}$	fuel-side (or waterside) micro-channel sidewall heat transfer rate
$q_{c,2}$	surface 2 convective heat transfer rate
$q_{c,3}$	surface 3 convective heat transfer rate
$q_{h,exp}$	measured airside heat transfer rate
$q_{h,th}$	theoretical airside heat transfer rate
$q_{h,1}$	surface 1 heat transfer rate
q''_s	heat flux across module's outer wall
R_A	thermal resistance of branch A of module's equivalent resistance
R_B	thermal resistance of branch B of module's equivalent resistance

$R_{c,2}$	surface 2 base convective resistance
$R_{c,3}$	surface 3 base convective resistance
R_{cond}	module's outer wall conduction resistance
$R_{c,sw1}$	first fuel (or water) sidewall resistance
$R_{c,sw2}$	second fuel (or water) sidewall resistance
$R_{h,1}$	airside resistance
$R_{h,4}$	airside base resistance
R_{tot}	total (equivalent) resistance
Re_c	fuel-side (or waterside) Reynolds number
$Re_{h,b}$	airside Reynolds number on back of module
$Re_{h,f}$	airside Reynolds number on finned side of module along fins
$Re_{h,uf}$	airside Reynolds number on finned side of module between fins
s_1	flow clearance above airside fin tip (0.0635 mm)
s_2	flow clearance along back of module (0.0635 mm)
T	temperature
T_1	surface 1 temperature
T_2	surface 2 temperature
T_3	surface 3 temperature
T_4	surface 4 temperature
T_c	fuel (or water) temperature
$T_{c,in,exp}$	measured waterside inlet temperature
$\bar{T}_{c,o}$	mean outlet fuel (or water) temperature
$T_{c,o,exp}$	measured waterside mean outlet temperature
$T_{c,o,th}$	theoretical waterside outlet temperature
T_h	air temperature
$T_{h,in,exp}$	measured airside inlet temperature
$\bar{T}_{h,o}$	mean outlet air temperature
$T_{h,o,exp}$	measured airside mean outlet temperature
$T_{h,o,th}$	theoretical airside mean outlet temperature
U	overall heat transfer coefficient
V_c	fuel-side (or waterside) mean velocity
V_h	airside mean velocity
W	width of module in direction of air flow
$W_{c,ch}$	fuel-side (or waterside) micro-channel width
$W_{c,w}$	fuel-side (or waterside) micro-channel wall thickness
$W_{h,ch}$	airside channel width
$W_{h,f}$	airside fin width
x	fuel (or water) direction coordinate
x'	dimensionless fuel (or water) direction coordinate
y	air direction coordinate
y'	dimensionless air direction coordinate

Greek symbols

$\delta_{h,f}$	airside finned boundary layer thickness
$\delta_{h,uf}$	airside unfinned boundary layer thickness
$\eta_{h,f}$	airside fin efficiency
θ	local dimensionless temperature difference between air and fuel (or water)
μ	dynamic viscosity
ν	kinematic viscosity
φ	ratio of mean to initial temperature difference

Subscripts

c	cold fuel stream (or simulated water stream)
h	hot air stream
s	solid surface

single module. The fuel is routed through a series of parallel micro- or mini-channels formed in a thin monolithic metallic structure. The fuel-side construction of the module is reminiscent of micro-channel heat sinks intended for cooling of high-heat-flux electronic chips as well as laser and radar devices [6]. Aside from their highly

compact and lightweight design, these devices greatly increase both heat transfer area to volume ratio and convective heat transfer coefficient on the fuel side. The new module design also enhances heat transfer on the airside with the use of short straight fins as illustrated in Fig. 1(a). The fins are formed in rows and
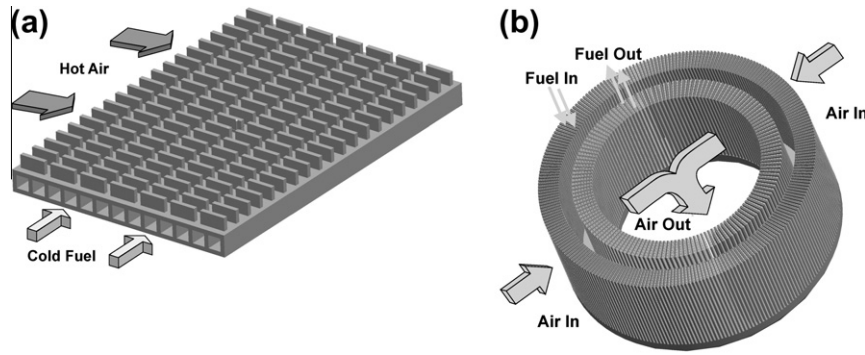
Fig. 1. (a) Cross-flow micro-channel air-to-fuel heat exchanger module. (b) Stacking of modules in radial in-flow turbine engine heat exchanger.

aligned with the airflow but perpendicular to the direction of the fuel flow. These fins enhance airside heat transfer in two ways. First, they greatly increase heat transfer area compared to a bare surface. Second, by using many short fins as opposed to continuous fins, they produce large heat transfer coefficients by reinitiating airside boundary layer development.

Another key advantage of the new module is that it allows the air–fuel heat exchanger to be configured in variety of design envelopes, such as annular or rectangular, depending on volume, weight or other constraints set by the engine manufacturer. Fig. 1(b) shows an annular design, in which the air is introduced radially inwards across two of radial stages of closely spaced cross-flow micro-channel modules. Not shown in this figure are the shared inlet and outlet headers for the modules.

The present study represents the first phase in the design of the air–fuel heat exchanger. A detailed analytical/numerical model is constructed to characterize the thermal performance of the heat exchanger module. Given the complexity in testing the perfor-

mance of the heat exchanger module using actual aircraft fuel, the model validation was assessed by substituting the fuel with water. The experimental facility developed for the study, the heat exchanger module construction and instrumentation, and experimental methods used are described in detail. Finally, experimental results and comparisons with the analytical/numerical predictions are presented.

2. Experimental methods

2.1. Test facility

The test facility developed for this project incorporated an air loop and a water loop to simulate, respectively, the air and fuel flows that the heat exchanger would encounter in a supersonic turbine engine. These loops are illustrated schematically in Fig. 2(a). In the air loop, compressed air flows through a series of filters to
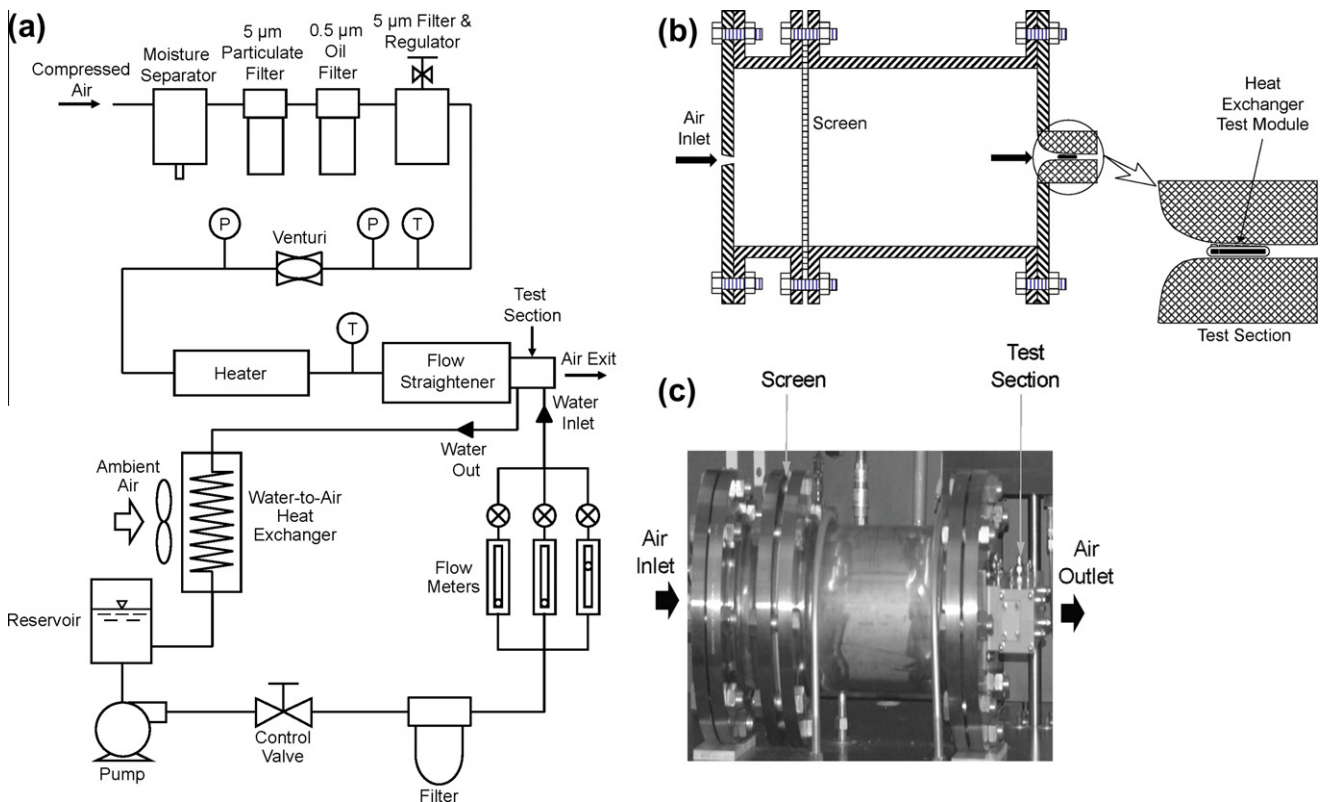

Fig. 2. (a) Schematic of flow loop and schematic (b) and photo (c) of flow straightener and test section.

remove any impurities such as water, oil, solid particulates. The air passes through a venturi flow meter to measure the air flow rate. Two different sonic venturis are used to provide broad coverage of flow rates. The air stream is heated by an inline heater to simulate air heating in a turbine engine, albeit at lower temperatures. A solid-state controller with an accuracy of ±2 °C is used to regulate the air temperature to the desired level between room temperature and 260 °C. Exiting the heater, the air enters a flow straightener to provide uniform flow at the inlet to the heat exchanger test module. The heated air converges through a nozzle before entering the test section containing the test module as illustrated in Fig. 2(b) and depicted in Fig. 2(c).

The water flow loop provides water flow that is regulated to the desired flow rate and temperature as it enters the test module. Illustrated in Fig. 2(a), the pump, reservoir, and water-to-air heat exchanger are all parts of an integral unit acquired from Lytron Inc. The filtered water is passed through one of three flow meters before entering the test module.

As shown in Fig. 3(a), the heat exchanger test module is contained in a PEEK plastic housing that provides thermal insulation for both the air and the water flows. Fig. 3(b) shows the location of the micro-channel heat exchanger module inside the PEEK housing and illustrates the paths of the air and the water streams in and out of the module.

2.2. Test module

Shown in Fig. 4, the test module was fabricated from stainless steel and measures 76.2 mm long and 15.24 mm wide. The airside fins cover one side of the test module excepting two 5.08 mm end regions of the same surface to allow a secure press fit into the insulating PEEK housing. Since the two end regions do not contribute to the heat transfer between the air and the water, the module simulates a 66.04 mm heat exchanger module in a turbine engine.

As illustrated in Fig. 4(a) and (b), the module's airside consists of 65 rows of fins. Each fin row consists of seven fins, six of which measure 1.524 mm while the middle fin measures 2.032 mm. The airside fin rows are angled to allow for a tighter packaging arrangement in an annular turbine heat exchanger design (see Fig. 1(b)). Fin height varies from 0.635 mm at the high edge to 0.127 mm at the lower, forming a 2.29° angle with the surface of the test module. As shown in Fig. 4(b), the waterside consists of 26 of 0.254 mm wide by 0.762 mm high micro-channels running the middle 66.04 mm of the test module's length.

While a module used in a gas turbine engine heat exchanger would likely be made of a nickel alloy to withstand the engine's high temperatures, the test module used in the present study was made of stainless steel because of its somewhat similar thermal conductivity and relative ease of machining compared to
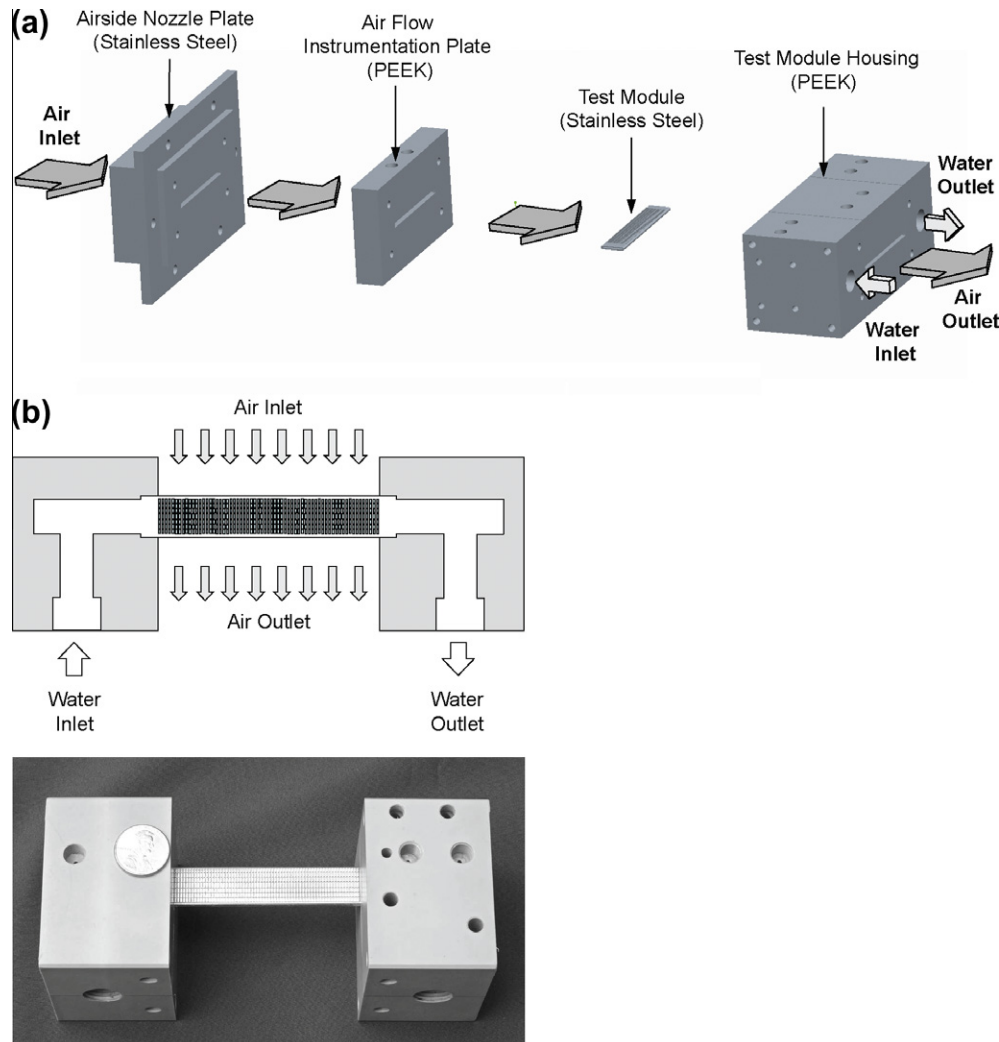

Fig. 3. (a) Exploded diagram of air nozzle and test module. (b) Air and water flow paths inside test module housing (middle portion of housing is removed to show micro-channel test module).
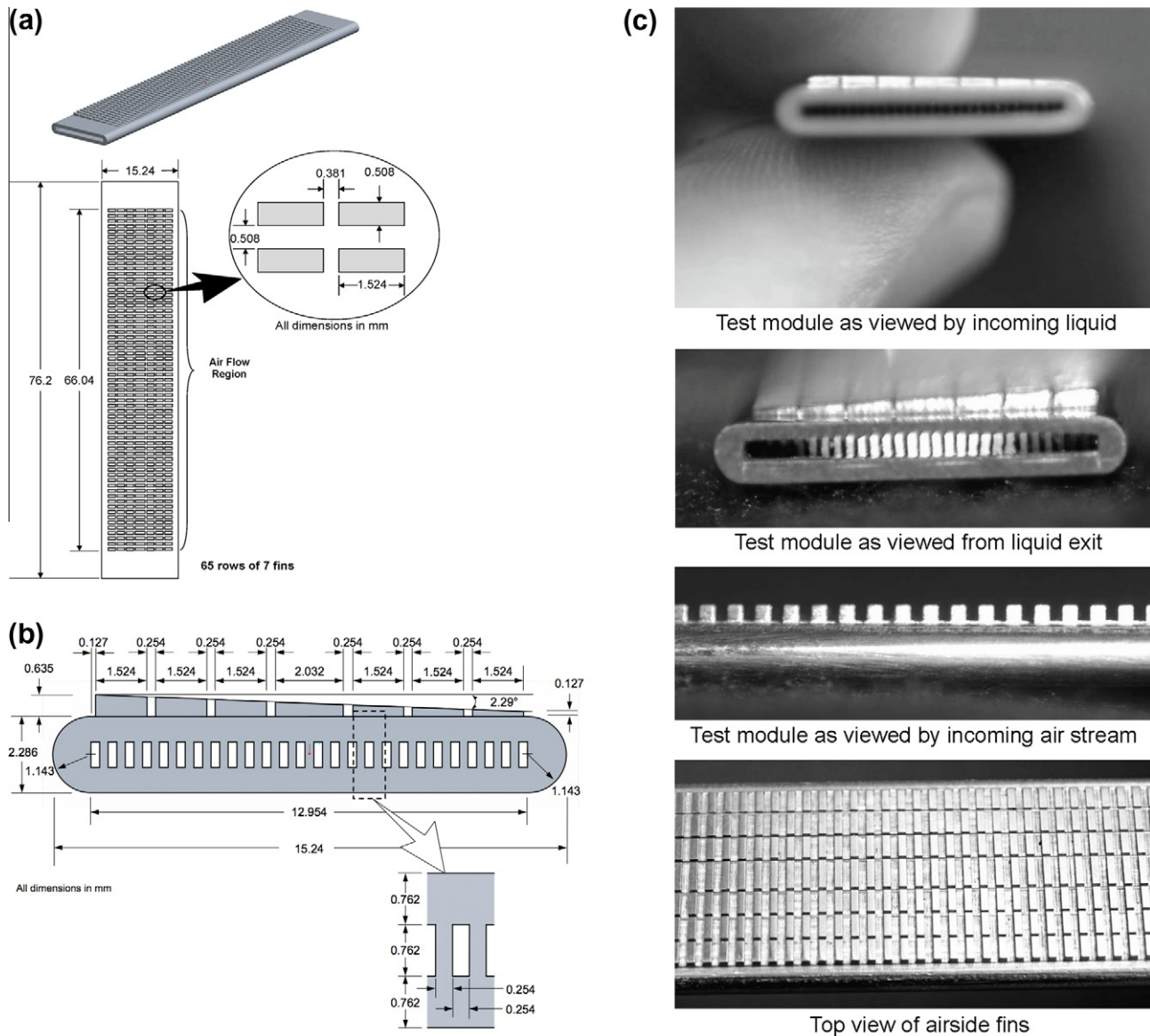
Fig. 4. Test module (a) airside geometry and (b) fuel-side and airside geometries. (c) Various views of test module.

nickel alloys. The test module was fabricated from two flat stainless steel plates. One was used to form a cover plate and the second the main body of the test module. The micro-channels were formed by holding the outer ends of the main plate in an aluminum fixture and cutting 0.762 mm deep parallel grooves using a series of miniature saw blades attached to an arbor, separated by thin spacers. The blade thickness equaled the width of the micro-channels, and the spacer thickness the width of solid wall between micro-channels, both 0.254 mm. A similar technique was used to form the airside fins.

With both stainless steel plates fabricated, the cover plate was soldered onto the base plate. The sides of the assembled module were rounded off to allow for more streamlined airflow around the module. It is important to note that the solder was applied to the base plate before the micro-channels were cut, leaving only the appropriate amount of solder on top of the fins. This prevented excess solder from running off and filling the micro-channels after machining. Fig. 4(c) shows photos of the completed test module.

2.3. Measurement accuracy

Type K thermocouples were used throughout the system and read by an Omega temperature indicator with an accuracy of ±0.5 °C. Temperatures were measured upstream of the venturi as well as upstream and downstream of both the air and water streams in the test module.

Pressures were measured by means of three absolute and three differential Druck pressure transducers, with accuracies of ±0.04% and ±0.25%, respectively, of the full-scale pressure reading. The transducers were used in tandem to record absolute pressure and pressure drop at three locations: across the venturi, across the airside of the test module, and across the waterside of the test module.

The two sonic venturis used to measure the air flow rates correspond to test module air velocities of 3–33 m/s. These meters are manufactured to ASME standards and possess an accuracy of ±1% of reading.

Three waterside flow meters were used to provide the required coverage over a broad range of flow rates. They had accuracies of

±6%, ±3%, and ±3%, respectively, over flow rate ranges of 0–441, 0–3784, and 0–18,930 cm^3/min.

3. Heat exchanger model

3.1. Overall heat exchanger modeling approach

The approach used to model the thermal performance of the air–fuel heat exchanger consists of first determining the temperature distributions for both the air and fuel streams across a single module. The method used here uses a mean overall heat transfer coefficient, U, between the air and the fluid streams that is assumed constant everywhere across the module. This coefficient is a function of the convective heat transfer coefficients for the air and the fluid, as well as the conduction resistances associated with the micro-channel plate and the air fins. Averaging the effects of the tapered air flow on the finned side of the test module will be discussed later.

Fig. 5 shows a schematic of a single module and the corresponding coordinate system and nomenclature. The complex geometrical features of the module are purposely omitted for now to help explain the differential model used to determine the temperature distributions of the two fluids. First, the temperatures of the hot air stream and cold fluid stream are defined, respectively, as

$$T_h = T_h(x,y) \tag{1a}$$

and

$$T_c = T_c(x,y). \tag{1b}$$

Under steady-state conditions, the rate of heat transfer between the air and the fluid across a heat exchanger differential area $dx\,dy$ is given by

$$dq = U(T_h - T_c)dx\,dy. \tag{2}$$

This rate is equal to both the differential sensible heat loss by the air and the differential sensible heat gain by the fluid across $dx\,dy$,

$$dq = -\left(\frac{\dot{m}_h}{L}\right)c_{p,h}\frac{\partial T_h}{\partial y}dx\,dy \tag{3a}$$

and

$$dq = +\left(\frac{\dot{m}_c}{W}\right)c_{p,c}\frac{\partial T_c}{\partial x}dx\,dy, \tag{3b}$$

where $\dot{m}_h$ and $\dot{m}_c$ are the mass flow rates of the air stream and the fluid stream, respectively, for the entire module. Eqs. (3a) and (3b) are based on the assumption that the flow rates are uniformly distributed for both fluid streams. These equations are also based on the assumption that all the heat lost by the air across the differential area is absorbed by the fluid; i.e., they assume both negligible heat loss and negligible axial conduction effects.

Mason [7] obtained a series solution for the dimensionless temperature difference θ between the air and the fluid as defined in Fig. 5 by combining and differentiating Eqs. (2), (3a), (3b), followed by the use of Laplace transforms.

$$\theta(x',y') = e^{-(ay'+bx')}\sum_{n=0}^{\infty}\frac{(abx'y')^n}{(n!)^2}, \tag{4}$$

where

$$a = \frac{UWL}{\dot{m}_h c_{p,h}} \tag{5a}$$

and

$$b = \frac{UWL}{\dot{m}_c c_{p,c}}. \tag{5b}$$

Integrating Eq. (2) over the entire surface area WL of the module yields an expression for the total heat transfer rate for the module,

$$q = U\int_{y=0}^{W}\int_{x=0}^{L}(T_h - T_c)dx\,dy$$
$$= UWL[T_h(0,0) - T_c(0,0)]\int_0^1\int_0^1\left(\frac{T_h - T_c}{T_h(0,0) - T_c(0,0)}\right)d\left(\frac{x}{L}\right)d\left(\frac{y}{W}\right). \tag{6}$$

Substituting the dimensionless definitions from Fig. 5 in Eq. (6) gives

$$\phi = \frac{q}{UWL[T_h(0,0) - T_c(0,0)]} = \int_0^1\int_0^1\theta dx'\,dy', \tag{7}$$

where ϕ is the ratio of mean outlet to inlet temperature difference. Using the solution for θ from Eq. (4), Eq. (7) can be expressed as

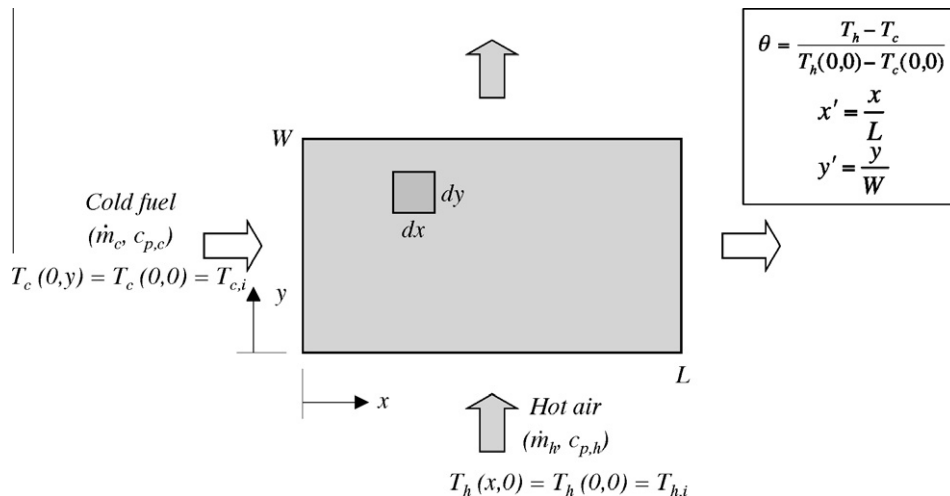**Fig. 5.** Schematic and nomenclature for cross-flow micro-channel heat exchanger module with uniform inlet fluid temperatures.

$$\phi = \int_0^1 \int_0^1 \theta \, dx' \, dy' = \int_0^1 \int_0^1 \left[e^{-(ay'+bx')} \sum_{n=0}^{\infty} \frac{(abx'y')^n}{(n!)^2} \right] dx' \, dy'$$

$$= \sum_{n=0}^{\infty} \left\{ \int_0^1 \int_0^1 \left[\frac{(abx'y')^n}{(n!)^2} e^{-(ay'+bx')} \right] dx' \, dy' \right\}. \tag{8}$$

The first integral of Eq. (8) can be rearranged as

$$\int_0^1 \left[\frac{(abx'y')^n}{(n!)^2} e^{-(ay'+bx')} \right] dx' = \int_0^1 \frac{(aby')^n}{(n!)^2} x'^n e^{-bx'} e^{-ay'} \, dx'$$

$$= \frac{(aby')^n}{(n!)^2} e^{-ay'} \int_0^1 x'^n e^{-bx'} \, dx'. \tag{9}$$

The solution for the integral in Eq. (9) can be found using integration tables [8]:

$$\int_0^1 x'^n e^{-bx'} \, dx' = e^{-bx'} \sum_{r=0}^{n} (-1)^r \frac{n! x'^{n-r}}{(n-r)!(-b)^{r+1}} \Bigg|_0^1$$

$$= e^{-b} \sum_{r=0}^{n} (-1)^r \frac{n!}{(n-r)!(-b)^{r+1}} - 1 \left[\frac{(-1)^n n!}{(-b)^{n+1}} \right]$$

$$= \frac{(-1)^n n!}{(-b)^{n+1}} \left[e^{-b} \sum_{r=0}^{n} \frac{b^{n-r}}{(n-r)!} - 1 \right] \tag{10}$$

Substituting the final answer from Eq. (10) into Eq. (8) and rearranging terms gives

$$\phi = \sum_{n=0}^{\infty} \left\{ \int_0^1 \frac{(aby')^n}{(n!)^2} e^{-ay'} \frac{(-1)^n n!}{(-b)^{n+1}} \left[e^{-b} \sum_{r=0}^{n} \frac{b^{n-r}}{(n-r)!} - 1 \right] dy' \right\}$$

$$= \sum_{n=0}^{\infty} \left\{ \frac{(ab)^n}{(n!)^2} \frac{(-1)^n n!}{(-b)^{n+1}} \left[e^{-b} \sum_{r=0}^{n} \frac{b^{n-r}}{(n-r)!} - 1 \right] \int_0^1 y'^n e^{-ay'} \, dy' \right\}. \tag{11}$$

The integral with respect to y' in Eq. (8) takes the same form as the integral with respect to x' and therefore can be solved using the same method.

$$\int_0^1 y'^n e^{-ay'} \, dy' = \frac{(-1)^n n!}{(-a)^{n+1}} \left[e^{-a} \sum_{r=0}^{n} \frac{a^{n-r}}{(n-r)!} - 1 \right]. \tag{12}$$

Substituting Eq. (12) into Eq. (11) and simplifying,

$$\phi = \sum_{n=0}^{\infty} \left\{ \frac{(ab)^n}{(n!)^2} \frac{(-1)^n n!}{(-a)^{n+1}} \frac{(-1)^n n!}{(-b)^{n+1}} \left[e^{-a} \sum_{r=0}^{n} \frac{a^{n-r}}{(n-r)!} - 1 \right] \left[e^{-b} \sum_{r=0}^{n} \frac{b^{n-r}}{(n-r)!} - 1 \right] \right\}$$

$$= \frac{1}{ab} \sum_{n=0}^{\infty} \left\{ \left[1 - e^{-a} \sum_{r=0}^{n} \frac{a^{n-r}}{(n-r)!} \right] \left[1 - e^{-b} \sum_{r=0}^{n} \frac{b^{n-r}}{(n-r)!} \right] \right\}. \tag{13}$$

Substituting k for $n - r$ yields the final solution

$$\phi = \frac{1}{ab} \sum_{n=0}^{\infty} \left[1 - e^{-a} \sum_{k=0}^{n} \frac{a^k}{k!} \right] \left[1 - e^{-b} \sum_{k=0}^{n} \frac{b^k}{k!} \right]. \tag{14}$$

Rearranging Eq. (7),

$$q = UWL[T_h(0,0) - T_c(0,0)]\phi. \tag{15}$$

Note that the module's total heat transfer rate must also equal the sensible heat lost by the hot stream or gained by the cold stream.

$$q = \dot{m}_h c_{p,h}[T_h(0,0) - \overline{T}_{h,o}] = \dot{m}_c c_{p,c}[\overline{T}_{c,o} - T_c(0,0)], \tag{16}$$

where $\overline{T}_{h,o}$ and $\overline{T}_{c,o}$ are the mean outlet temperatures of the hot stream and the cold stream, respectively. Combining Eqs. (15) and (16) and introducing the definitions of a and b from Eqs. (5a) and (5b), respectively, yield the following relations for the mean outlet temperatures.

$$\overline{T}_{h,o} = T_h(0,0) - a[T_h(0,0) - T_c(0,0)]\phi \tag{17a}$$

and

$$\overline{T}_{c,o} = T_c(0,0) + b[T_h(0,0) - T_c(0,0)]\phi. \tag{17b}$$

In summary, the performance parameters of the heat exchanger module consist of total heat transfer rate, q, which can be determined from Eq. (15), outlet temperature of the hot stream, $\overline{T}_{h,o}$, from Eq. (17a), and outlet temperature of the cold stream, $\overline{T}_{c,o}$, from Eq. (17b). Calculating these three parameters requires determining a and b from Eqs. (5a) and (5b), respectively, and φ from Eq. (14).

3.2. Overall heat transfer coefficient

The only unknown in the parameter a in Eq. (5a) and b in Eq. (5b) is the overall heat transfer coefficient, U. This parameter can be determined by using a thermal resistance network using the heat exchanger module geometry illustrated in Fig. 6(a). On one surface of the module, the air flows over the external fins as well as along the surface between the fins. The air also flows over the back surface of the module. The fluid travels through the micro-channels. Details of the airside and fluid-side boundaries are given in Fig. 6(b) and (c). The number of airside fin rows, $N_{h,f}$, and fuel-side micro-channels, $N_{c,ch}$, can be found using the following relations

$$N_{h,f} = \frac{L}{W_{h,ch} + W_{h,f}} \tag{18a}$$

and

$$N_{c,ch} = \frac{W}{W_{c,ch} + W_{c,w}}, \tag{18b}$$

respectively.

For the finned airside, the heat is transferred through finned and unfinned portions of the surface. Introducing the definition of airside fin efficiency [9], the heat transfer rate for the finned surface (surface 1) of the module can be expressed as

$$q_{h,1} = q''_{h,1}(WL) = q_{h,f} + q_{h,uf}$$

$$= N_{h,f} \eta_{h,f} \bar{h}_{h,f} A_{h,f}(T_h - T_1) + N_{h,f} \bar{h}_{h,uf} A_{h,uf}(T_h - T_1)$$

$$= N_{h,f}(\eta_{h,f} \bar{h}_{h,f} A_{h,f} + \bar{h}_{h,uf} A_{h,uf})(T_h - T_1), \tag{19}$$

where

$$A_{h,f} = N_{h,r}[2(W_{h,f} + L_{h,f})H_{h,f} + W_{h,f} L_{h,f}], \tag{20}$$

$$A_{h,uf} = (W_{h,f} + W_{h,ch})W - N_{h,r} W_{h,f} L_{h,f}, \tag{21}$$

$\eta_{h,f}$ is the airside fin efficiency, $\bar{h}_{h,f}$ and $\bar{h}_{h,uf}$ are the average airside heat transfer coefficients for the fin and base surfaces, respectively, $A_{h,f}$ and $A_{h,uf}$ are the areas of the fin and base surfaces in a single fin row, respectively, and $N_{h,r}$ is the number of airside fins in each row of fins.

Rearranging Eq. (19) yields

$$q_{h,1} = \frac{T_h - T_1}{\left\{ \frac{1}{N_{h,f}[\eta_{h,f} \bar{h}_{h,f} A_{h,f} + \bar{h}_{h,uf} A_{h,uf}]} \right\}}, \tag{22}$$

which is used to determine the airside resistance as

$$R_{h,1} = \frac{1}{N_{h,f}[\eta_{h,f} \bar{h}_{h,f} A_{h,f} + \bar{h}_{h,uf} A_{h,uf}]}. \tag{23}$$

For the fluid side, the heat must first travel through the outer metallic wall of the micro-channels, which has a thickness $H_{c,w}$ and conductivity k_s as illustrated in Fig. 6(c). Assuming the inner surface temperature of the outer wall, T_2, is uniform, and the conduction across the outer wall one-dimensional,
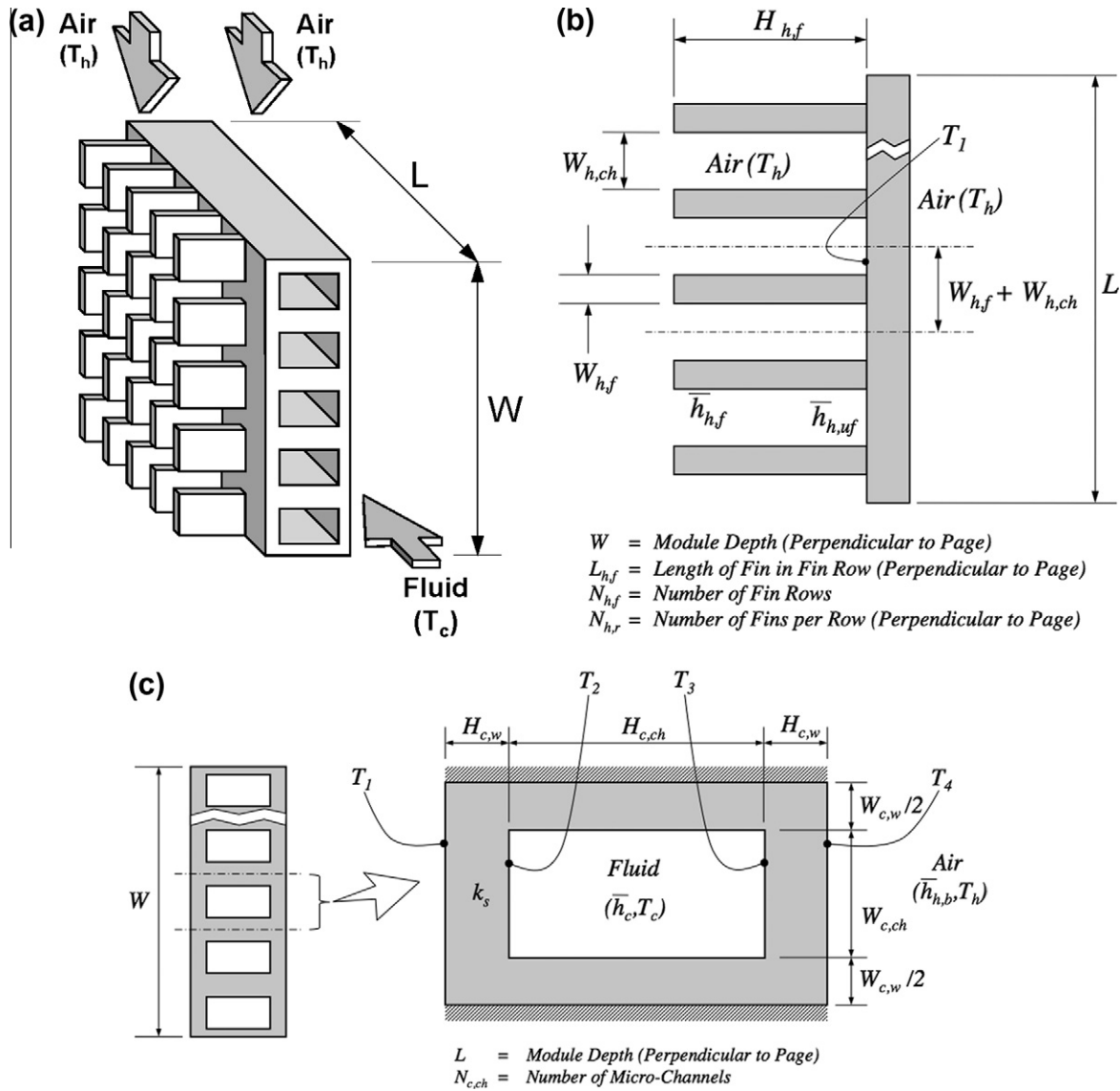
Fig. 6. Schematics and nomenclature of (a) heat exchanger module, (b) finned airside boundary and (c) fuel micro-channels and unfinned airside boundary.

$$q_s''(LW) = k_s(LW)\frac{T_1 - T_2}{H_{c,w}} = \frac{T_1 - T_2}{\left\{\frac{H_{c,w}}{k_s(LW)}\right\}},$$ (24)

Eq. (24) yields the following relation for thermal resistance of the outer wall,

$$R_{cond} = \frac{H_{c,w}}{k_s(LW)}.$$ (25)

The micro-channel sidewalls can be approximated as fins. Using a prescribed fin tip temperature case (see [9]), the rate of heat flow through the sidewalls can be broken into the difference between two separate heat flow terms.

$$q_{c,sw} = N_{c,ch}\sqrt{\bar{h}_c P_{c,f} k_s A_{c,csf}}(T_2 - T_c)\frac{\left[\cosh(m_c H_{c,ch}) - \frac{T_3 - T_c}{T_2 - T_c}\right]}{\sinh(m_c H_{c,ch})}$$

$$= N_{c,ch}\sqrt{\bar{h}_c P_{c,f} k_s A_{c,csf}}(T_2 - T_c)\coth(m_c H_{c,ch}) - N_{c,ch}$$

$$\times \sqrt{\bar{h}_c P_{c,f} k_s A_{c,csf}}(T_3 - T_c)\csc h(m_c H_{c,ch}),$$ (26)

where

$$P_{c,f} = 2L,$$ (27a)

$$A_{c,csf} = W_{c,w}L$$ (27b)

and

$$m_c = \sqrt{\frac{\bar{h}_c P_{c,f}}{k_s A_{c,csf}}}.$$ (27c)

Eq. (26) may be rearranged as

$$q_{c,sw} = \frac{T_2 - T_c}{\left\{\frac{1}{N_{c,ch}\sqrt{\bar{h}_c P_{c,f} k_s A_{c,csf}}\coth\left(\sqrt{\frac{\bar{h}_c P_{c,f}}{k_s A_{c,csf}}}H_{c,ch}\right)}\right\}}$$

$$- \frac{T_3 - T_c}{\left\{\frac{1}{N_{c,ch}\sqrt{\bar{h}_c P_{c,f} k_s A_{c,csf}}\csc h\left(\sqrt{\frac{\bar{h}_c P_{c,f}}{k_s A_{c,csf}}}H_{c,ch}\right)}\right\}}$$ (28)

to yield the following two expressions for fluid sidewall resistances,

$$R_{c,sw1} = \frac{1}{N_{c,ch}\sqrt{\bar{h}_c P_{c,f} k_s A_{c,csf}} \coth\left(\sqrt{\frac{\bar{h}_c P_{c,f}}{k_s A_{c,csf}}} H_{c,ch}\right)} \tag{29a}$$

and

$$R_{c,sw2} = \frac{1}{N_{c,ch}\sqrt{\bar{h}_c P_{c,f} k_s A_{c,csf}} \operatorname{csc} h\left(\sqrt{\frac{\bar{h}_c P_{c,f}}{k_s A_{c,csf}}} H_{c,ch}\right)}. \tag{29b}$$

Aside from the sidewalls, there is direct convective heat transfer from surface 2 of the micro-channel to the fluid.

$$q_{c,2} = N_{c,ch}\bar{h}_c(W_{c,ch}L)(T_2 - T_c) = \frac{(T_2 - T_c)}{\left\{\frac{1}{N_{c,ch}\bar{h}_c(W_{c,ch}L)}\right\}}, \tag{30}$$

which yields the following expression for base convective resistance

$$R_{c,2} = \frac{1}{N_{c,ch}\bar{h}_c(W_{c,ch}L)}. \tag{31}$$

Similarly, there is direct convection for surface 3 of the micro-channel to the fluid, which is associated with a similar convective resistance.

$$q_{c,3} = N_{c,ch}\bar{h}_c(W_{c,ch}L)(T_3 - T_c) = \frac{(T_3 - T_c)}{\left\{\frac{1}{N_{c,ch}\bar{h}_c(W_{c,ch}L)}\right\}} \tag{32}$$

and

$$R_{c,3} = \frac{1}{N_{c,ch}\bar{h}_c(W_{c,ch}L)}. \tag{33}$$

The heat must flow from the opposite hot airside through the other wall of the micro-channel, whose conductive resistance is identical to that given by Eq. (25).

On the backside of the heat exchanger module, heat is transferred from the air to the back surface by convection.

$$q_{a,b} = \bar{h}_{h,b}(WL)(T_h - T_4) = \frac{(T_h - T_4)}{\left\{\frac{1}{\bar{h}_{h,b}(WL)}\right\}}, \tag{34}$$

which yields the following expression for convective resistance

$$R_{h,4} = \frac{1}{\bar{h}_{h,b}(WL)}. \tag{35}$$

The total heat transfer between the air and the fluid for the entire module can be related to both the module's total thermal resistance, R_{tot}, and the overall heat transfer coefficient, U.

$$q''(WL) = \frac{T_h - T_c}{R_{tot}} = U(WL)(T_h - T_c), \tag{36}$$

which yields

$$U = \frac{1}{(WL)R_{tot}}. \tag{37}$$

As shown in Fig. 7, the total resistance may be represented as the equivalent of two parallel branches A and B. Each branch consists of a series of three resistances; the third of which is the equivalent of two parallel resistances. Therefore,

$$R_{tot} = \frac{R_A R_B}{R_A + R_B}, \tag{38a}$$

where

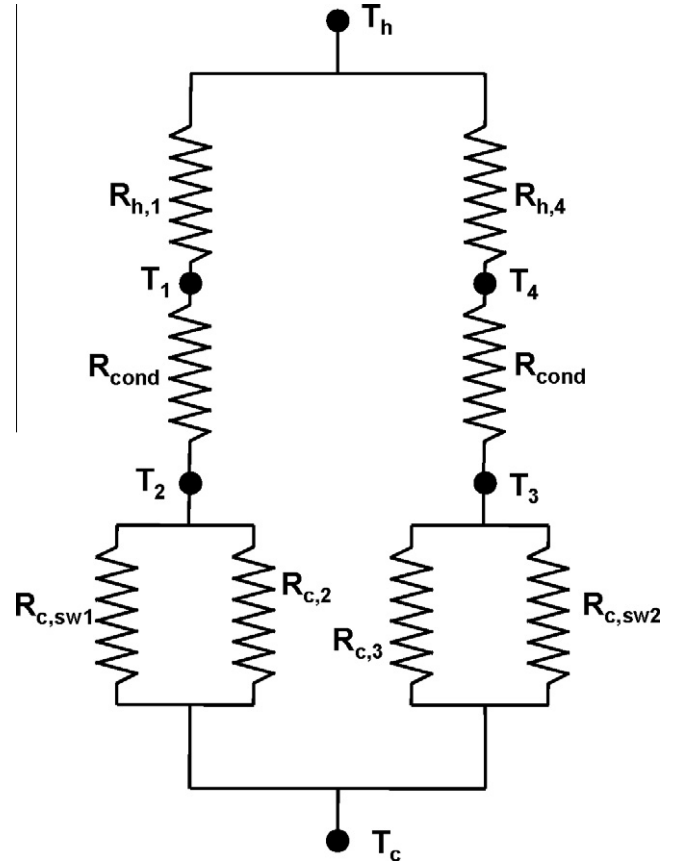$$R_A = R_{h,1} + R_{cond} + \frac{R_{c,sw1}R_{c,2}}{R_{c,sw1} + R_{c,2}} \tag{38b}$$

and

Fig. 7. Equivalent thermal resistance network representing entire micro-channel module.

$$R_B = R_{h,4} + R_{cond} + \frac{R_{c,cw2}R_{c,3}}{R_{c,cw2} + R_{c,3}}. \tag{38c}$$

3.3. Determination of airside and fluid side heat transfer coefficients and fin efficiencies

Eq. (37) shows that calculating the overall heat transfer coefficient requires determination of the airside and fluid-side heat transfer coefficients as well as fin efficiencies. To accomplish this task, the module geometry, the air and fluid inlet conditions, and the air and fluid properties must be initialized. In the present study, water was used to simulate the fuel stream. The air and water properties were determined using EES [10].

In the airside fin calculations, laminar flow over a flat plate is assumed, based on the low Reynolds numbers associated with the present application and the experimental validation study. For this assumption to be valid for the entire air passage between two adjacent rows of fins, the boundary layer thickness must be smaller than the spacing between fin rows. Otherwise, the boundary layers would merge, and the air flow would resemble internal instead of external flow. The airside fin efficiency can be determined by using the approximation for a fin with an adiabatic tip because $\bar{h}_{h,f}W_{h,f}/k_s \leqslant 0.0625$ for the present study. Laminar flow over a flat plate is also assumed for the airside base calculations between fins. As with the airside fins, this assumption is valid if the boundary layers for the base and the adjacent module (or PEEK housing in the experimental study) do not merge, which would change the flow from external to internal.

Unlike the finned side, the air flow along the back of the module (surface 4 in Fig. 6(c)) is internal, given the small back flow

clearance s_2. Here, a correlation for laminar flow in a channel with an equivalent hydraulic diameter is used.

The fuel-side convection coefficient is determined from correlations for flow in a circular channel that are corrected for equivalent hydraulic diameter of the micro-channel. For laminar flow conditions of interest, two different correlations are recommended based on Prandtl number range.

Table 1 provides all correlations or relations for the airside and fluid-side heat transfer coefficients and fins [9] that are used to evaluate the overall heat transfer coefficient U. It should be noted that a viscosity ratio term that appears in the heat transfer coefficient correlations in Table 1 was set equal to unity in the present study.

4. Experimental results and comparison with model predictions

As discussed earlier, water was used to simulate aircraft fuel in a high Mach gas turbine engine. Experiments were performed to assess the performance of the module over a range of air and water flow rates. The air flow rate was set by a combination of air temperatures and pressures upstream of the venturi. The water flow rate was measured by one of three water flow meters.

Fig. 8 shows the measured outlet airside temperature profile for a fixed inlet air temperature and fixed flow rate and four water flow rates. Notice that the air temperature is lowest at $x = 0$ (see Fig. 5), where the water is coolest, and highest at $x = L$, where the
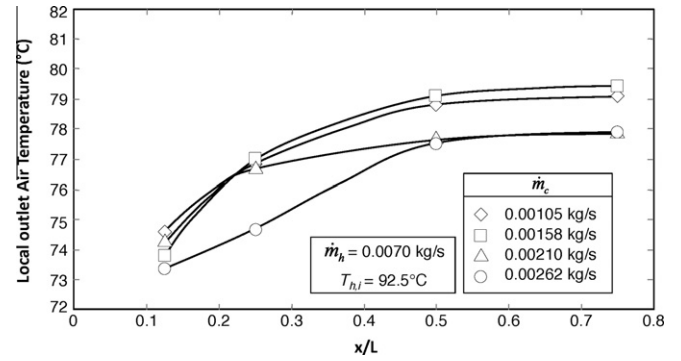

Fig. 8. Outlet air temperature profiles for different water flow rates.

water is warmest. Also, notice the gradient of the airside temperature profile is strongest near $x = 0$, especially near $y = 0$, where local heat transfer rate between the air and the water is greatest.

Since the airside fins are tapered, with the tallest fin at the air inlet and becoming progressively shorter, the values that are functions of air fin height—such as air velocity and air fin efficiency—vary across the module. To arrive at an average value for the overall heat transfer coefficient, U, for the test module and compare the model predictions to the test module results, an average fin height is used. Since the height of the air fins changes linearly, the average

Table 1
Heat transfer coefficient and fin efficiency equations.

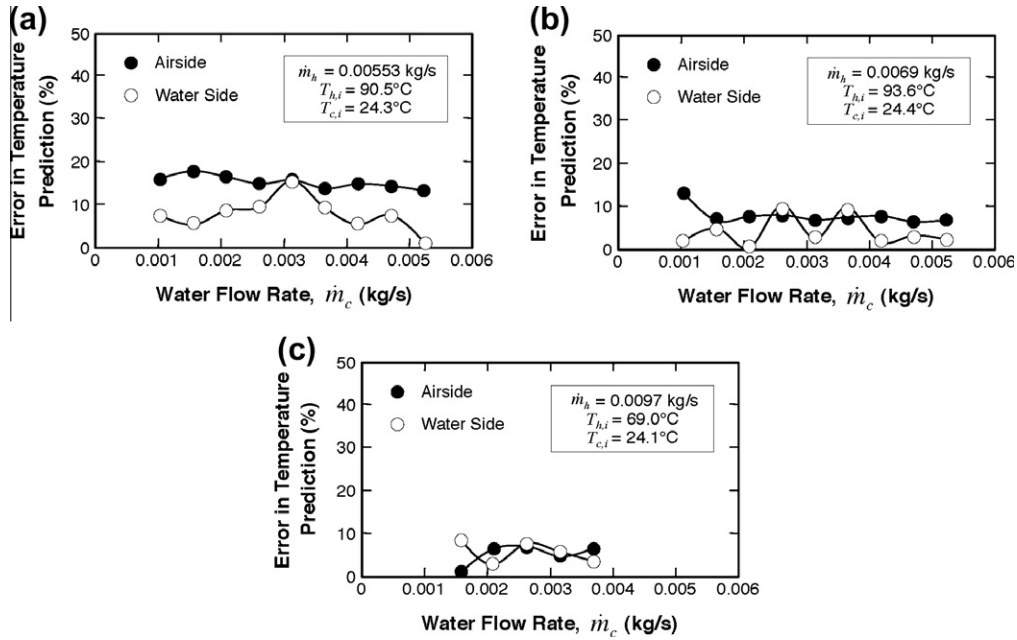| Module section	Equation
Air flow on finned side of module along fins	Heat transfer coefficient:
	$$\overline{Nu}_{h,f} = \frac{\bar{h}_{h,f}L_{h,f}}{k_h} = 0.664 Re_{h,f}^{1/2} Pr_h^{1/3}$$
	where $Re_{h,f} = \frac{V_h L_{h,f}}{v_h}$, valid for $\delta_{h,f} < W_{h,ch}/2$, $Re_{h,f} < 5 \times 10^5$ and $Pr_h > 0.6$
	Fin efficiency:
	$$\eta_{h,f} = \frac{\tanh(m_h H_{h,fe})}{m_h H_{h,fe}}$$
	where
	$$H_{h,fe} = H_{h,f} + W_{h,f}/2, \quad m_h = \sqrt{\frac{\bar{h}_{h,f}P_{h,f}}{k_s A_{h,csf}}}, \quad P_{h,f} = 2(W_{h,f} + L_{h,f}), \quad A_{h,csf} = W_{h,f}L_{h,f}$$
Air flow on finned side of module between fins	Heat transfer coefficient:
	$$\overline{Nu}_{h,uf} = \frac{\bar{h}_{h,uf}W}{k_h} = 0.664 Re_{h,uf}^{1/2} Pr_h^{1/3}$$
	where $Re_{h,uf} = \frac{V_h W}{v_h}$ valid for $\delta_{h,uf} < (H_{h,f} + s_1)/2$, $Re_{h,uf} < 5 \times 10^5$ and $Pr_h > 0.6$
Fluid flow in micro-channels	Heat transfer coefficient:
	$$\overline{Nu}_c = \frac{\bar{h}_c D_{c,eq}}{k_c} = 3.66 + \frac{0.0668\left(\frac{D_{c,eq}}{L}\right)Re_c Pr_c}{1 + 0.04[(\frac{D_{c,eq}}{L})Re_c Pr_c]^{2/3}} \text{ for } Re_c < 2300 \text{ and } Pr_c \geq 5$$
	$$\overline{Nu}_c = \frac{\bar{h}_c D_{c,eq}}{k_c} = 1.86\left(\frac{Re_c Pr_c}{L/D_{c,eq}}\right)^{1/3}\left(\frac{\mu_c}{\mu_{c,s}}\right)^{0.14} \text{ for } Re_c < 2300 \text{ and } Pr_c < 5$$
	where $Re_c = \frac{V_c D_{c,eq}}{v_c}$, $D_{c,eq} = \frac{4(W_{c,ch}H_{c,ch})}{2(W_{c,ch}+H_{c,ch})}$
Airflow on back of module	Heat transfer coefficient:
	$$\overline{Nu}_{h,b} = \frac{\bar{h}_{h,b}D_{eq,b}}{k_h} = 1.86\left(\frac{Re_{h,b}Pr_h}{W/D_{h,eq}}\right)^{1/3}\left(\frac{\mu_h}{\mu_{h,s}}\right)^{0.14} \text{ for } Re_{h,b} < 2300 \text{ and } Pr_h < 5$$
	where $Re_{h,b} = \frac{V_h D_{h,eq}}{v_h}$, $D_{h,eq} = 2s_2$

Fig. 9. Percent error in predicting airside and waterside temperature drop with water flow rate for (a) $\dot{m}_c = 0.00553$ kg/s, $T_{h,i}$ = 90.5 °C, and $T_{c,i}$ = 24.3 °C, (b) $\dot{m}_c = 0.0069$ kg/s, $T_{h,i}$ = 93.6 °C, and $T_{c,i}$ = 24.4 °C, and (c) $\dot{m}_c = 0.0097$ kg/s, $T_{h,i}$ = 69.0 °C, and $T_{c,i}$ = 24.0 °C.

fin height is the height of the fin in the middle of the module. Therefore, the terms calculated from the average fin height are essentially values for the middle of the module.

Fig. 9 shows the percent error in predicting the temperature drop across the air and water streams for three sets of operating conditions. For the airside, the percent temperature error is defined as

$$\% \; Airside \; temperature \; error = \frac{|T_{h,o,\exp} - T_{h,o,th}|}{(T_{h,in,\exp} - T_{h,o,\exp})}, \tag{39}$$
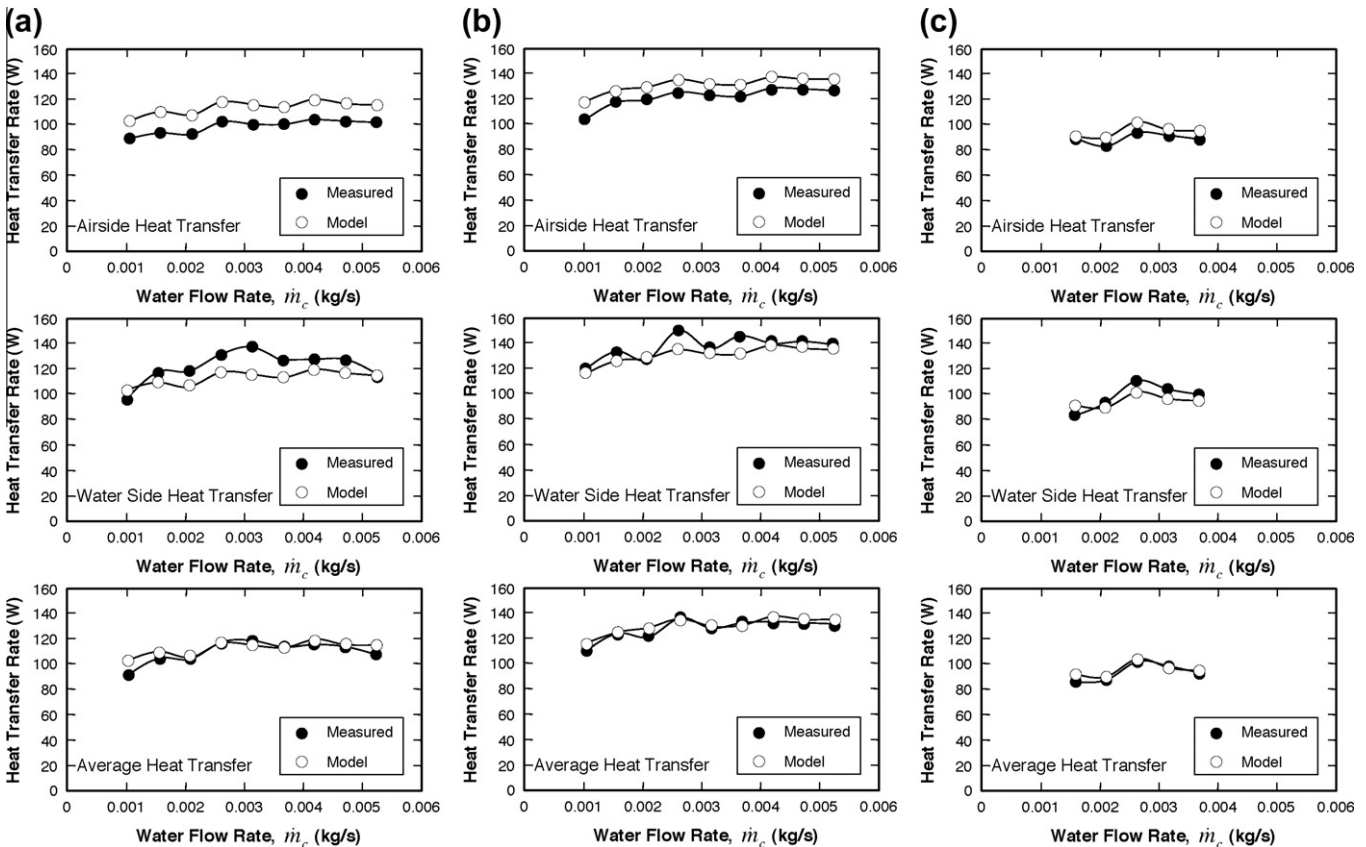

Fig. 10. Comparison of predicted and measured heat transfer rate for airside, waterside and average of two sides with water flow rate for (a) $\dot{m}_c = 0.00553$ kg/s, $T_{h,i}$ = 90.5 °C, and $T_{c,i}$ = 24.3 °C, (b) $\dot{m}_c = 0.0069$ kg/s, $T_{h,i}$ = 93.6 °C, and $T_{c,i}$ = 24.4 °C, and (c) $\dot{m}_c = 0.0097$ kg/s, $T_{h,i}$ = 69.0 °C, and $T_{c,i}$ = 24.0 °C.
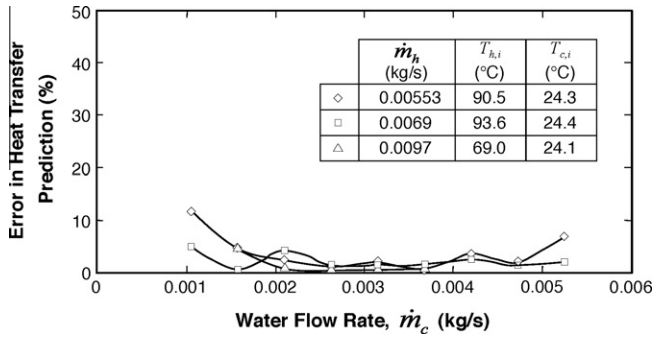
Fig. 11. Percent error in predicting average heat transfer rate versus water flow rate for different operating conditions.

where $T_{h,in,exp}$, $T_{h,o,exp}$, and $T_{h,o,th}$ are the measured inlet temperature, the measured mean outlet temperature, and the predicted mean outlet temperature, respectively. Similarly, the percent temperature error for the waterside is defined as

$$\% \ Waterside \ temperature \ error = \frac{|T_{c,o,\exp} - T_{c,o,th}|}{(T_{c,o,\exp} - T_{h,in,\exp})}, \qquad (40)$$

where $T_{c,in,exp}$, $T_{co,exp}$, and $T_{c,o,th}$ are the measured inlet temperature, the measured mean outlet temperature, and the predicted mean outlet temperature, respectively. Fig. 9 shows errors for both the air- and watersides are mostly below 10% for the two higher airside flow rates but increase to about 15% for the lowest airside flow rate, where venturi measurement error is greatest. These errors may be related to several factors. First, there are uncertainties associated with the various instruments used such as the venturis and the water flow meters. Also, there were slight fluctuations in the water flow rate, which created added difficulty in pinpointing the exact water flow rate and caused slight fluctuations in the air outlet temperature. Third, the model calculations are based on an average fin height for the finned airside of the test module, which introduces some error in predicting the module performance. Nonetheless, the small error values in Fig. 9 support the overall accuracy of the heat exchanger model.

The module's heat transfer rates are measured and calculated for the cold and hot streams, respectively, as

$$q_c = \dot{m}_c c_{p,c} (\overline{T}_{c,o} - T_{c,i}) \qquad (41a)$$

and

$$q_h = \dot{m}_h c_{p,h} (T_{h,i} - \overline{T}_{h,o}). \qquad (41b)$$

Fig. 10 compares predicted and measured heat transfer rates for the waterside and airside calculated according to Eqs. (41a) and (41b), respectively. These results show good agreement in both magnitude and trend. There is an increase in overall heat transfer rate between Fig. 10(a) and (b) mostly because of the increasing air flow rate. An appreciable decrease in the heat transfer rate between Fig. 10(b) and (c) appears to be mostly the result of the large decrease in air inlet temperature despite the higher air flow rate.

To further assess the accuracy of the model predictions of the module's heat transfer rate, the following error parameter is defined,

$$\% \ Heat \ transfer \ rate \ error = \frac{\left| \left(\frac{q_{h,\exp} + q_{c,\exp}}{2}\right) - \left(\frac{q_{h,th} + q_{c,th}}{2}\right) \right|}{\left(\frac{q_{h,\exp} + q_{c,\exp}}{2}\right)}. \qquad (42)$$

Fig. 11 shows good agreement between model and experiment, with values for all except one test falling below 10% error.

These results demonstrate the effectiveness of the model as a tool for both the design and performance assessment of cross-flow micro-channel heat exchangers.

5. Conclusions

This paper explored the design, analysis and performance assessment of a new class of heat exchanger intended for high Mach gas turbine engines. While the actual application will involve dissipating the heat from hot compressor air to aircraft fuel, the fuel in the present experiments was simulated using water. Key findings from the study are as follows:

(1) A new cross-flow micro-channel heat exchanger, which consists of a number of closely spaced modules, was designed. Within each module, the fuel flows through a series of parallel micro-channels, while the air flows externally over rows of short, straight fins perpendicular to the direction of fuel flow. This compact design is well suited for aircraft applications where weight and volume are primary design concerns.
(2) A new theoretical model, which consists of a cross-flow heat exchanger submodel, an internal micro-channel fluid flow submodel, a resistance network submodel, and associated correlations and models for heat transfer coefficients and fins efficiencies, was constructed. The overall model is shown to provide closure in predicting outlet temperatures and heat transfer rates for the two fluid streams.
(3) Comparisons between theory and experiment show good agreement in both exit temperatures and heat transfer rates. This proves the model is a reliable tool for predicting the module's performance under actual turbine engine conditions and for the design of aircraft heat exchangers of different sizes and design envelopes.

References

[1] Rolls-Royce, The Jet Engine, fifth ed., Rolls-Royce plc, Derby, England, 1996.
[2] G.B. Bruening, W.S. Chang, Cooled Cooling Air Systems for Turbine Thermal Management, ASME Paper No. 99-GT-14.
[3] H. Huang, L.J. Spadaccini, D.R. Sobel, Fuel-cooled thermal management for advanced aero engines, J. Eng. Gas Turbines Power 126 (2004) 284–293.
[4] T.P. Kibbey, Impinging Jets for Application in High-Mach Aircraft Thermal Management, M.S. Thesis, Purdue University, West Lafayette, IN, 2004.
[5] N.R. Herring, S.D. Heister, On the use of wire coil inserts to augment tube heat transfer, J. Enhanced Heat Transfer 16 (2009) 19–34.
[6] I. Mudawar, Assessment of high-heat-flux thermal management schemes, IEEE Trans. Compon. Pack. Technol. 24 (2001) 122–141.
[7] J.L. Mason, Heat transfer in crossflow, in: Proceedings of Second US National Congress of Applied Mechanics, Ann Arbor, MI, 1954, pp. 801–803.
[8] W.H. Beyer, Standard Mathematical Tables, 24th ed., CRC Press, Cleveland, OH, 1976.
[9] F. Incropera, D. Dewitt, T. Bergman, A. Lavine, Fundamentals of Heat and Mass Transfer, sixth ed., Wiley, Hoboken, New Jersey, 2007.
[10] S.A. Klein, Engineering Equation Solver (EES), F-Chart Software, Madison, WI.